Ideal vitrification, barrier hopping, and jamming in fluids of modestly anisotropic hard objects

Galina Yatsenko and Kenneth S. Schweizer*

Department of Materials Science and Frederick Seitz Materials Research Laboratory, University of Illinois, 1304 West Green Street, Urbana, Illinois 61801, USA

(Received 24 June 2007; published 26 October 2007)

Our recent theory for the glassy dynamics of fluids and suspensions of hard nonspherical objects is applied to several modestly anisotropic shapes. The role of bond length and aspect ratio is studied for diatomics, triatomics, and spherocylinders. As spherical symmetry is broken the ideal kinetic glass transition volume fraction of all objects increases linearly with aspect ratio with the same slope, in surprising agreement with the jamming phase diagram of hard granular ellipsoids. The ideal glass boundary of all shapes is a nonmonotonic function of aspect ratio which is also in qualitative accord with the jamming behavior of spherocylinders and ellipsoids. The maximum glass volume fraction shifts to higher values, and larger aspect ratios, as the object becomes smoother. Suggestions for why the nonequilibrium jamming and kinetic ideal glass formation (dynamical crossover) boundaries are similar are advanced. Beyond the ideal glass volume fraction the nonequilibrium free energy acquires a localization well and entropic barrier. Although its form is highly nonuniversal, if different shapes are compared at constant barrier height then a good collapse is found. Collapse of the volume fraction dependence of the barrier height for different shapes is also predicted for modest shape anisotropy, but increasingly fails as the aspect ratio exceeds 2. For a given volume fraction the mean barrier hopping times are nonmonotonic functions of aspect ratio. The functional form of this dependence, and order of magnitude variation with aspect ratio, is distinct for each object.

DOI: 10.1103/PhysRevE.76.041506 PACS number(s): 64.70.Pf, 61.43.Fs, 61.20.Gy, 47.57.−s

I. INTRODUCTION

The glassy dynamics of fluids and suspensions of hard nonspherical objects is of significant experimental and theoretical interest in both molecular [1] and colloid [2] science. The first principles ideal mode coupling theory (MCT) [3] has been extended to hard diatomic molecules at the site level [4] and to ellipsoids of revolution at the center of mass and Euler angle level [5]. Interesting predictions have been made, including a nonmonotonic dependence of the ideal glass volume fraction and diffusion constant on particle shape which is supported by computer simulations [6,7]. However, MCT predicts a kinetic transition to a fully nonergodic solid state which is not realized in practice due to ergodicity restoring activated barrier hopping processes. This aspect has motivated us and our collaborators to propose a stochastic nonlinear Langevin equation theory [8,9] that addresses barrier formation and activated transport, including dynamic non-Gaussian fluctuation effects that are poorly accounted for by the standard ideal MCT [10]. Theories for hard sphere colloidal suspensions and fluids [8,10,11], hard diatomics [12], colloidal gels [13,14], and polymer melts [15–17] and glasses [18–20] have been developed and extensively confronted with experiment and computer simulation.

The focus of this paper is to extend our recent theory of hard diatomics [12] to several modestly anisotropic shapes of both a discrete site and continuous geometrical nature. Possible connections between ideal glass transitions and the nonthermal jamming of granular objects are also explored. Remarkable similarities between the nonmonotonic dependence of the jamming [21–23] and ideal kinetic glass boundaries on particle aspect ratio have been discovered, and ideas for their physical origin are presented.

Our approach to describing the slow dynamics of nonspherical objects is based on a dynamical preaveraging of orientational degrees of freedom resulting in a center-of-mass description of soft repulsive particles [12]. Here we show this approach can be alternatively motivated as a reduced description at the site level which suggests a real space collision perspective of the theory. The latter has been extensively developed for hard spheres based on an analytic "ultralocal limit" of the barrier hopping theory [24].

We study modestly anisotropic hard objects that do not form liquid crystals: two-site diatomics and three-site triatomics of variable bond lengths and spherocylinders (Fig. 1). A primary goal is to disentangle the effect of nonsphericity as quantified by an aspect ratio from smaller scale geometric features (e.g., particle smoothness or surface corrugation). The diatomic and spherocylinder (triatomic) are characterized by two (three) length scales. The dynamical theory is recalled in Sec. II and pair correlation function and structure factor calculations are presented. Insights concerning the physical content of the approach are given in Sec. III. Section IV presents the naive MCT glass boundaries which are contrasted in Sec. V with the jamming phase diagrams of spherocylinders and ellipsoids. Section VI studies the object shape dependent localization length, entropic barrier, and mean hopping time, and conclusions are drawn in Sec. VII.

II. THEORY

The present work employs the theoretical approach of Ref. [12]. Here we briefly recall the key prior results.

A. Structural correlations

Consider an arbitrarily shaped rigid object composed of N spherical interaction sites [25,26] of the *same* diameter (D)

*kschweiz@uiuc.edu

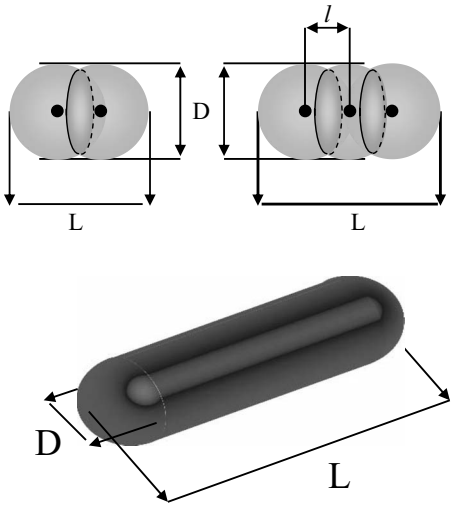

FIG. 1. Diatomic, triatomic, and spherocylinder. L/D is the overall aspect ratio and the bond length between neighboring sites is l.

which are either rigorously symmetry equivalent (e.g., homonuclear diatomic) or taken to be approximately equivalent (e.g., a site-averaged description of a triatomic). Diatomics and triatomics are characterized by a bond length l and an overall length-to-diameter (aspect) ratio L/D. As described previously [27], a spherocylinder is modeled in the site representation as a continuous limit of N sites of diameter D and bond length l where $N\to\infty$, $l\to 0$, and $Nl=L-D$. The intermolecular site-site pair correlation functions are computed based on the reference interaction site model (RISM) theory [25]. Under the site equivalency simplification RISM theory consists of a single scalar integral equation which in Fourier transform space is given by [25,26]

$$h_{ss}(k) = \omega_{ss}(k)C_{ss}(k)\omega_{ss}(k) + \rho_s\omega_{ss}(k)C_{ss}(k)h_{ss}(k). \quad (1)$$

Here $\rho_s=Nn/V=N\rho$ is the site number density, n the number of particles in a volume V, ρ the molecular number density, $h_{ss}(k)$ is the Fourier transform of the intermolecular site-site total correlation function $h_{ss}(r)=g_{ss}(r-1)$, $C_{ss}(r)$ is the intermolecular site-site direct correlation function, and $\omega_{ss}(k)$ is the intramolecular structure factor

$$\omega_{ss}(k) = N^{-1}\sum_{\alpha,\gamma=1}^{N}\omega_{\alpha\gamma}(k), \quad (2)$$

where $\omega_{\alpha\gamma}(k)$ is Fourier transform of the probability distribution function for sites α and γ. For hard core interactions the site-site Percus-Yevick (PY) closure is [25,28]

$$C_{ss}(r) = 0, \quad r > D. \quad (3)$$

The site-site total structure factor that quantifies collective density fluctuations is

$$S_{ss}(k) \equiv \omega_{ss}(k) + \rho_s h_{ss}(k) = \frac{1}{\omega_{ss}^{-1}(k) - \rho_s C_{ss}(k)}. \quad (4)$$

The system is dynamically described at the center-of-mass (CM) level. The CM and site level total structure factors are related by adopting the "rigid particle" approximation [29] discussed in depth previously [12],

$$S_{ss}(k) \cong \omega_{ss}(k)S_{CM}(k). \quad (5)$$

At the CM level the Ornstein-Zernike relation of an atomic liquid applies [28],

$$S_{CM}(k) = 1 + \rho h_{CM}(k) = \frac{1}{1 - \rho C_{CM}(k)}. \quad (6)$$

Comparing Eqs. (5) and (6) yields

$$C_{CM}(k) = N\omega_{ss}(k)C_{ss}(k), \quad (7)$$

$$h_{CM}(k) \equiv \frac{N}{\omega_{ss}(k)}h_{ss}(k), \quad (8)$$

which are equivalent statements of the rigid particle mapping. For $k\to 0$ one has

$$S_{CM}(k=0) \equiv S_{CM,0} = \rho k_B T\kappa_T = \frac{S_{ss,0}}{N}, \quad (9)$$

where κ_T is the isothermal compressibility [28].

The intramolecular structure factors of a rigid diatomic or triatomic can be trivially written down [12,25] and are normalized such that $\omega_{ss}(k=0)=N$. For a continuous spherocylinder the intramolecular structure factor is a line, which in the "form factor" representation $[\omega_{ss}(k=0)\equiv 1]$ is given by the well-known expression [30]

$$\omega_{ss}(k) = 2\frac{Si(qL)}{qL} - 4\frac{\sin^2(qL/2)}{(qL)^2}, \quad (10)$$

where $Si(x)\equiv\int_0^x dy y^{-1}\sin(y)$. The rewriting of the RISM equation for an object composed of a continuous distribution of sites of diameter D is given elsewhere [27].

B. Naive MCT and activated hopping dynamics theory

The central dynamic order parameter is the scalar displacement of the *center of mass* from its initial position, $r(t)$, which obeys a closed nonlinear stochastic Langevin equation of motion [9]. In the overdamped limit the Langevin equation is given by [8,9]

$$\zeta_S\frac{\partial r(t)}{\partial t} = -\frac{\partial F_{eff}(r(t))}{\partial r(t)} + \delta f(t), \quad (11)$$

where $\zeta_S=k_BT/D_S$ is a short time friction constant and the random thermal force satisfies $\langle\delta f(0)\delta f(t)\rangle=2k_BT\zeta_S\delta(t)$. The key quantity is the nonequilibrium or effective free energy, $F_{eff}(r(t))$, which describes within a local equilibrium dynamic density functional framework the effect of surrounding particles on the tagged colloid dynamics. In terms of the CM variables and in units of k_BT it is given by [8,9]

$$F_{eff}(r) = F_{ideal} + F_{excess}$$
$$= -3\ln(r) + \int\frac{d\vec{k}}{(2\pi)^3}\frac{\rho C_{CM}^2(k)S_{CM}(k)}{1+S_{CM}^{-1}(k)} \times\exp\left\{-\frac{k^2r^2}{6}(1+S_{CM}^{-1}(k))\right\}. \quad (12)$$

Minimization of Eq. (12) with respect to r, or solution of Eq. (11) in the absence of noise, or solving an approximate Gaussian theory for the mean square displacement (MSD), all yield [9] the naive MCT self-consistent equation (with a de Gennes narrowing correction) for the long time limit of the MSD or localization length r_{loc} [8,31],

$$r_{loc}^{-2} = \frac{1}{9}\int \frac{d\vec{k}}{(2\pi)^3}\rho k^2 C_{CM}^2(k) S_{CM}(k) e^{-(k^2 r_{loc}^2/6)[1+S_{CM}^{-1}(k)]}. \tag{13}$$

The emergence of the first noninfinite solution of Eq. (13) for r_{loc} defines the ideal glass transition volume fraction, ϕ_c. It signals a qualitative change in the nonequilibrium free energy to a form characterized by a localization well and barrier, and thus a crossover to activated dynamics. The mean first passage or barrier hopping time follows in the high friction overdamped (diffusive barrier crossing) limit from Kramers theory [8,32]

$$\frac{\tau}{\tau_s} = \frac{2\pi}{\sqrt{\tilde{K}_0 \tilde{K}_B}} e^{F_B/k_B T}, \tag{14}$$

where $\tau_s = D^2\zeta_s/k_B T$ for hard spheres, ζ_s is the short time friction constant, F_B the barrier height, and $\tilde{K}_0$ and $\tilde{K}_B$ are the absolute magnitudes of the well and barrier harmonic curvatures in units of $k_B T/D^2$, respectively.

C. Real and reciprocal space structure

Examples of the CM intermolecular pair correlation function for triatomics at a fixed volume fraction (the hard sphere naive MCT glass transition) and various aspect ratios are shown in Fig. 2(a). The contact value trends at the site and CM levels are qualitatively the same. The corresponding CM structure factors are shown in Fig. 2(b). *All features on all length scales are nonmonotonic functions of aspect ratio*. This includes $S_{CM}(k=0) \equiv S_{0,CM}$ which quantifies molecular number density fluctuations, the intensity of the wide angle peak that quantifies the coherence of local cage order, $S_{CM}(k^*) = S_{CM}^*$, and its corresponding length scale $2\pi/k^*$. This nonmonotonic behavior reflects enhanced packing disorder of objects characterized by three different local length scales (D, l, L) when L/D is close to unity. The inset demonstrates the nonmonotonic variations are property (length scale) specific. These structural features play the key role in quantifying cage constraints and glassy dynamics.

III. VERTEX, FORCES, AND COLLISIONS

A. Vertex

The central input to the dynamical theory is a length scale resolved "vertex,"

$$V_{CM}(k) \equiv k^4 \rho C_{CM}^2(k) S_{CM}(k). \tag{15}$$

This quantity represents a Fourier-resolved *effective* total mean square force on the object CM including the surface area integration factor (k^2). It enters the naive MCT, Eq. (13), and effective force (derivative of the nonequilibrium free energy) in Eq. (11). As discussed previously [12,24], the vertex amplitude approaches a constant at large wave vectors. Hence, the r dependence of $F_{eff}(r)$, and the r_{loc} dependence of the naive MCT self-consistent equation (13), are significantly influenced by large wave vector contributions. This feature has motivated the formulation and detailed analysis of an ultralocal analytic limit of the theory [24].

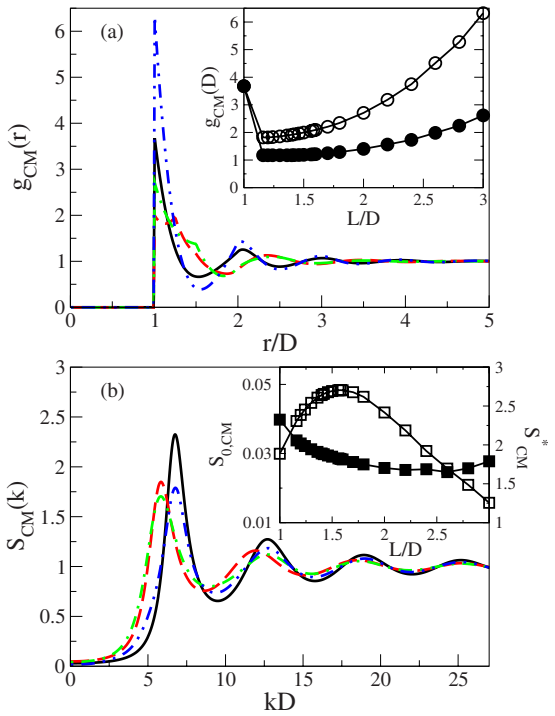

FIG. 2. (Color online) (a) CM-CM intermolecular pair correlation functions of triatomic fluids as a function of scaled separation for a volume fraction of $\phi=0.432$. Aspect ratios are $L/D=1$ (solid), 1.5 (dashed), 2 (dot-dashed) and 3 (dot-dot-dashed). The inset shows the contact value at the CM level [open circles, defined as $g_{CM}(r=D)$] and at the site-site level (solid circles) as a function of aspect ratio L/D. The curves are guides to the eye. (b) Analogous collective structure factors as a function of scaled wave vector. The inset shows the $k=0$ value or dimensionless compressibility (open squares, left vertical axis) and the cage peak intensity (solid squares, right vertical axis) as a function of aspect ratio L/D.

Figure 3 shows representative examples of the vertex. The generic behavior for all shapes, aspect ratios, and (high) volume fractions of interest is an essentially constant amplitude for wave vectors beyond the first two oscillations. The latter occur on the length scales of roughly one (cage) and two site diameters. Both naive MCT and its barrier hopping generalization involve contributions from force fluctuations on all scales via the integral over k in Eqs. (12) and (13). The Debye-Waller-like factors provide the natural high wave vector cutoff [12,24], and their corresponding length scale defines the most relevant force fluctuations which are sensitive to object shape and volume fraction.

B. Mean squared force on the center of mass

The underlying idea of our approach is to first map the site level description of the hard object structural correlations

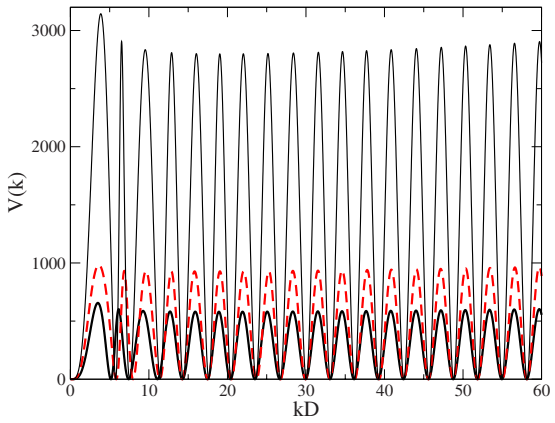

FIG. 3. (Color online) High wave vector limit of the CM vertex (in units of $1/D$) as a function of dimensionless wave vector at volume fractions of 0.432 (lowest curve) and 0.62 (upper curve) for a $L/D=1.4$ diatomic. The dashed curve is for a $L/D=2$ diatomic at $\phi=0.432$.

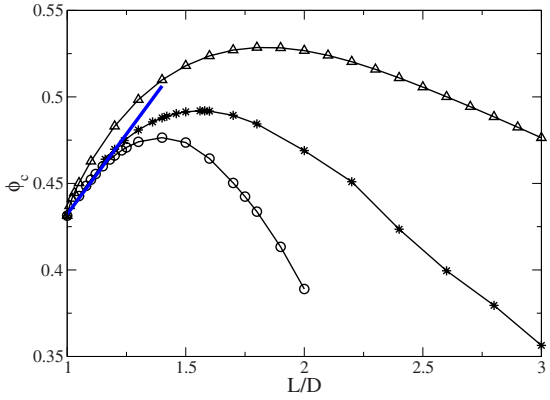

FIG. 4. (Color online) Ideal glass transition volume fraction as a function of aspect ratio for diatomic (circles), triatomic (stars), and spherocylinder (triangles) fluids. The initial linear common form for the diatomic and triatomic is indicated. The linear behavior is well described by the function $0.18\ L/D+0.25$, which is accurate up to $L/D\sim 1.22$.

to a reduced center-of-mass level [12]. Then the dynamics is assumed to be the same as a soft sphere fluid with structural correlations given by the object shape and volume fraction dependent structure factor and direct correlation function. Here we point out an alternative interpretation which makes contact with prior efforts to develop a MCT of entangled polymer melts and dense solutions [33].

First rewrite Eq. (15) at the site level using Eqs. (5)–(7),

$$V_{CM}(k) = k^4 N \rho_s C_{ss}^2(k)\omega_{ss}(k)S_{ss}(k). \tag{16}$$

One can define a matrix quantity that represents the contribution due to forces exerted by the surroundings on sites i and j of a tagged molecule,

$$V_{ij}(k) = k^2 \sum_{m,l=1}^{N} [kC_{im}(k)]\rho S_{ml}(k)[kC_{lj}(k)]\omega_{ij}(k), \tag{17}$$

$$V_{CM}(k) = \sum_{i,j=1}^{N} V_{ij}. \tag{18}$$

This form suggests the alternative view that our approach computes the total mean square force on the CM of an object within a site representation where the usual factorization of multipoint correlations [3,33] to the two point level is adopted. The idea of first constructing the CM correlations from the site description, followed by a soft sphere mapping for dynamics, need not be literally invoked. Moreover, Eq. (16) is of the form of the zero time CM memory function, $N\Sigma_f$, of the polymer MCT [33].

It is of interest to examine the constant vertex amplitude at high wave vectors. The single molecule and collective structure factors approach unity at large k, and the quantity $kC_{ss}(k)$ is proportional to the Fourier transform of the effective site-site intermolecular force. An elementary consequence of the RISM integral equation is that for hard sites $C_{ss}(r)$ must have a jump discontinuity at contact of magnitude given by the site level contact value, $g_{ss}(D)$ [24,25]. These facts then imply

$$V_{CM}(k) \underset{k\to\infty}{\to} \sum_{i=1}^{N} V_{ii}(k)|_{k\to\infty} = k^2 \sum_{m,l=1}^{N} [kC_{im}(k)]\ \rho[kC_{li}(k)]|_{k\to\infty}$$
$$\approx k^4 N \rho_s C_{ss}^2(k\to\infty) \propto N\rho_s g_{ss}^2(D). \tag{19}$$

The limiting vertex amplitude is thus determined by the number of sites and contact value squared which quantifies an effective mean square repulsive force associated with sites interacting via a renormalized force dC_{ss}/dr. To the extent the high wave vector part of the vertex dominates the numerical predictions of the theory, Eq. (19) provides a real space collision picture [24]. However, especially near an ideal glass boundary, quantitative deviations of the theory from its ultralocal limit due to vertex contributions on the cage and larger scales, and also explicit intramolecular bonding constraints [via ω_{ss}(k) in Eq. (6) and (7)], may be important as discussed below.

IV. IDEAL VITRIFICATION OF TRIATOMICS AND SPHEROCYLINDERS

A. Ideal glass boundary

The CM naive MCT glass transition boundaries for diatomics, triatomics, and spherocylinders are shown in Fig. 4. As discussed previously [12] the diatomic result is in qualitative agreement with the more sophisticated full ideal MCT studies [4,5]. Each ideal glass boundary displays a nonmonotonic variation with aspect ratio. As spherical symmetry is initially broken the glass transition is suppressed, i.e., pushed to higher volume fractions. The initial increase of the glass volume fraction is linear in aspect ratio with a slope that appears to be essentially identical for different shapes. This common behavior seems remarkable given spherical geometry is continuously broken for the discrete site models in

contrast to the spherocylinder which is characterized by a singular change of geometry [34,35]. Apparently at small degrees of anisotropy differences in corrugation between the three shapes are irrelevant.

At a system-specific degree of anisotropy the ideal glass boundary goes through a maximum. The values of L/D and volume fraction of this "most difficult to vitrify" state increases from diatomics to triatomics to spherocylinders. Hence, as the object becomes smoother, and has less "dead volume" in the crevices defined by overlapping bond interaction sites, it is harder to vitrify based on the standard definition of fluid volume fraction. The glass volume fraction at the "end point" geometry ($L/D=2$ or 3) also increases as the object becomes smoother. Both the triatomic and spherocylinder have ideal glass volume fractions at $L/D=3$ higher than the hard sphere, in contrast to the glass boundary of the diatomic system.

B. Origin of trends and controlling variables

An interesting question is whether a variable related to packing and degree of fluid order can be identified which correlates with the rich nonmonotonic and shape-specific behavior of the ideal glass boundaries. We have previously shown for diatomics that the amplitude of the wide angle peak of $S(k)$, although a nonmonotonic function of L/D, does not correlate well with the ideal glass boundary shape within the naive MCT approach [12]. The same conclusion applies to triatomics and spherocylinders [see inset of Fig. 2(b)]. However, $S_{0,CM} \equiv S_0$, the dimensionless isothermal compressibility, was empirically found to be nearly invariant along the diatomic ideal glass boundary [12]. The vertex calculations (Fig. 3) show a limiting high wave vector amplitude plateau for all systems and conditions examined, and hence one can also ask whether its amplitude mimics the shape of the ideal glass boundaries in Fig. 4.

Results for S_0, the vertex amplitude evaluated at the CM cage peak and its high wave vector analog as a function of aspect ratio are shown in Fig. 5(a) for the diatomic fluid at a fixed volume fraction. The analogous results for the spherocylinder and triatomic are given in Fig. 5(b). All these quantities are nonmonotonic functions of aspect ratio. The behavior of the vertex at high k and the cage peak are extremely similar. At a detailed level, the vertex for the diatomic has a maximum essentially exactly where its ideal glass volume fraction peaks. Even subtle aspects of the shape-dependence of the vertex amplitude are consistent with the glass boundary, such as it being larger at $L/D=2$ than for hard spheres. The story for the triatomic is essentially identical. For spherocylinders the location of the vertex maximum is well aligned with the maximum glass volume fraction aspect ratio, and its value at $L/D=3$ is consistent with the glass boundary occurring at a volume fraction significantly larger than for hard spheres. All the qualitative trends described for the high wave vector vertex amplitude also apply for the $k=0$ quantity S_0.

Thus, at a semiquantitative level the behavior of the ideal glass boundaries follows directly from the nonmonotonic dependence of S_0 or the vertex amplitudes on object anisotropy

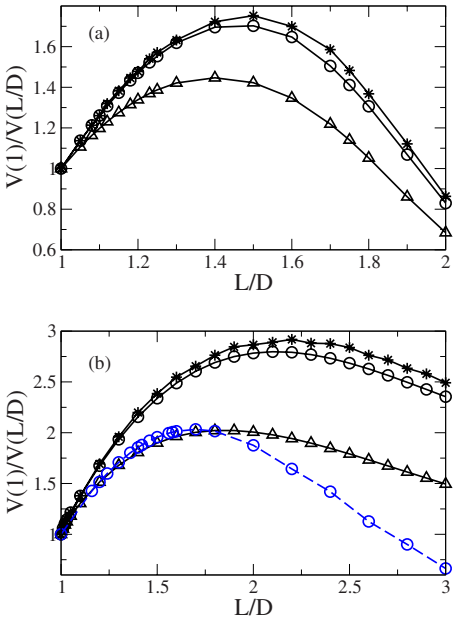

FIG. 5. (Color online) Ratio of the hard sphere to nonspherical object vertex as a function of aspect ratio at $\phi=0.432$. Results at k^* (stars) and the limiting high wave vector regime ($kD=[30,60]$; circles) are shown for the diatomic (a) and spherocylinder (b). Results for the triatomic and $kD \gg 1$ are also shown in panel (b) as the dashed curve through the open circles. Triangles indicate $S_0(L/D)$ for the diatomics (a) and spherocylinder (b) normalized to unity for $L/D=1$ (hard sphere).

thereby providing a simple physical interpretation. Figure 6 explores a more demanding test by asking whether there is a "conserved variable" along the glass line. The vertex amplitude along the ideal glass boundaries for all shapes overlaps well. Moreover, for $L/D<1.4$ the collapse is essentially exact. However, the vertex amplitude varies significantly (roughly linearly) with L/D. Additional factors play a role in determining the aspect ratio dependence of the glass boundaries. The candidates are obvious: L/D-*dependent* cage scale correlations and explicit bonding constraints via $\omega_{ss}(k)$.

Figure 6 also demonstrates that the results for the real space parameter of Eq. (19) are nearly identical to the trends of the high wave vector vertex calculations as expected theoretically. We have also examined the ratio of the amplitude of the vertex at high wave vectors to the quantity of Eq. (19) (not plotted). It is remarkably flat beyond a rather low $L/D \sim 1.3$ for diatomics and triatomics, but increases linearly by 15% as the hard sphere state is approached.

Finally, Fig. 6 empirically demonstrates that S_0 is an excellent conserved variable along the glass boundary. The constancy is nearly exact at lower aspect ratios where the glass boundary is linear for all shapes. However, as emphasized in our prior diatomic work [12], and recent analytic analysis for hard spheres [24], one should not conclude that it is $k \sim 0$ fluctuations that control the glassy physics. Rather it is local structural correlations that matter and the proper deduction is these force constraints have amplitude that correlates with the dimensionless compressibility. Small deviations from a constant S_0 do emerge as the glass boundary

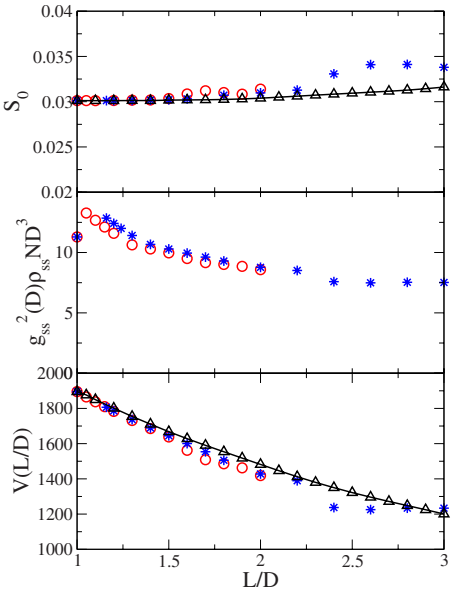

FIG. 6. (Color online) Values of three quantities along the ideal glass boundary as a function of aspect ratio for the diatomic (circles), triatomic (stars), and spherocylinder (triangles). The upper panel shows the dimensionless compressibility at the CM level. The middle panel is dimensionless parameter $g_{ss}^2(r=D)N\rho_s D^3$ identified in Eq. (19) as quantifying the high wave vector limit of the vertex. The bottom panel shows the limiting high wave vector amplitude of the vertex (units of $1/D$). The smooth curves drawn through the spherocylinder results are a guide to the eye.

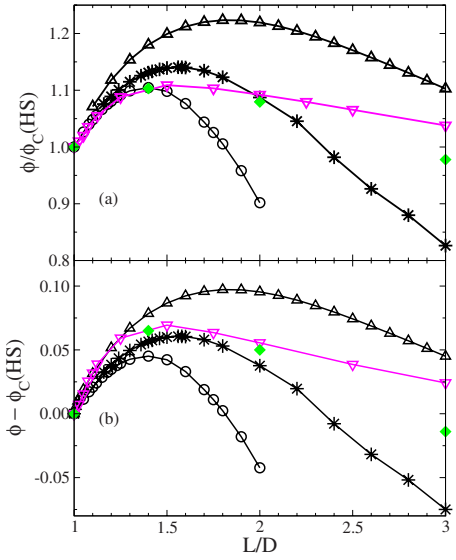

FIG. 7. (Color online) Comparison of the ideal glass transition boundary for diatomics (circles), triatomics (stars), and spherocylinders (upward triangles) to the simulation determined jamming boundary of granular prolate ellipsoids (downward triangles) [34] based on two different normalizations to the hard sphere limit: a ratio format (a) and a difference format (b). Jamming results for hard spherocylinders [23] are indicated as solid diamonds.

goes through it maximum, especially for the triatomic. Ultimately for the $L/D \gg 1$ long rod case the glass boundaries do not occur in a dense fluid regime, and additional deviations from a constant S_0 behavior occur as will be discussed elsewhere.

V. COMPARISON TO THE JAMMING TRANSITION

The athermal mechanical jamming of hard oblate and prolate ellipsoids [21,22,34] and spherocylinders [23] has been recently studied using computer simulation. A striking nonmonotonic dependence of the maximum random close packing volume fraction on shape anisotropy was discovered. From a mathematical perspective ellipsoids of revolution and spherocylinders are very different [34,35], however their nonmonotonic jamming curves are quite similar. In the jamming problem the key issue is the discontinuous emergence of a true interparticle contact network. In contrast, the kinetic ideal MCT glass transition of a fluid does not involve literal contacts between particles (statistically these are of measure zero) and is based on equilibrium structural input. Nevertheless, our present and prior results [12], and more advanced ideal MCT calculations for hard diatomics [4] and ellipsoids of revolution [5], have found nonmonotonic variations of the glass boundary that look seductively similar to the jamming phase diagrams.

To compare the results of Fig. 4 with the jamming studies we have replotted them in Fig. 7 normalized to the critical volume fraction of the reference hard sphere system. The representation of Fig. 7(a) is the format adopted in recent jamming studies of granular ellipsoids [34]. The behavior of prolate and oblate ellipsoids was found to be nearly identical [34] and results for only the former are shown. Clearly the normalized jamming phase diagram is not precisely the same as the ideal glass transition boundaries. Given the different shapes studied and questions asked this seems unavoidable. But we find the similarities to be significant and surprising. For example, the initial linear form of the boundaries, including the precise slope, is essentially identical for the ideal glass and ellipsoid jamming curves, and the location of the maxima are also close. These similarities are even more apparent in Fig. 7(b) which adopts an alternative normalization. The ellipsoid curve is intermediate between the theoretical analog for the triatomic and spherocylinder, which seems natural from a geometrical perspective. Note the actual volume fractions for hard spheres are very different for the ideal glass (0.432) and the random close packing (RCP) state ($\sim$0.64). This makes any correspondence even more intriguing. Jamming results for hard spherocylinders [23] are also shown in Fig. 7. Precise agreement with the analogous ideal glass boundary does not occur, but all the qualitative features again agree.

The question remains why there might be a connection between the ideal glass boundary, which is controlled by local packing considerations of an equilibrium compressible fluid and the onset of dynamical localization, and the nonequilibrium jamming transition defined by the emergence of a contact network and static shear modulus. We do not have a definite answer but feel that summarizing recent results and offering speculations pertinent to this fascinating issue is worthwhile. Mathematical analysis has recently yielded an

understanding of why the jamming boundary is linear at very small degrees of anisotropy [35]. However, we find essentially identical behavior, and the underlying physics is unquestionably different. The "excluded volume caging" perspective that MCT describes has been advanced by some [23,36] for understanding the jamming transition. It seems undoubtably correct for highly anisotropic objects such as long rods, but when the anisotropy is modest has been disputed (e.g., ellipsoids) [34]. From our viewpoint, the qualitative similarities of the ideal glass boundaries of diatomics, triatomics, and spherocylinders, coupled with the common behavior for the jamming of prolate and oblate ellipsoids and spherocylinders, suggests the excluded volume driven caging perspective has significant merit.

As suggested by Torquato [37], perhaps the similar nonmonotonic form of the jamming and ideal glass boundaries is related to the fact that each boundary quantifies when a property vanishes and another undergoes a discontinuous change. For jamming it is the isothermal compressibility that vanishes and the number of interparticle contacts jumps from zero to nonzero. At the ideal MCT glass transition there is a "bifurcation" of the nonequilibrium free energy. If the random noise required to escape over a barrier is ignored [9] this corresponds to a true nonergodic transition where particle mobility goes to zero and the long time inverse localization length (or Debye-Waller factor) jumps from zero to a nonzero value. This interpretation of the ideal MCT glass transition is attractive since granular materials are non-Brownian and thermal fluctuations irrelevant by definition. Interestingly, study of the random sequential adsorption (RSA) transition in hard particles also shows a nonmonotonic dependence of the critical volume fraction on object aspect ratio [34,38] that is qualitatively the same as the jamming and ideal glass boundaries. In RSA what vanishes is the probability for particle insertion which occurs at volume fractions commensurate with the ideal glass boundaries and far below RCP. Finally, we note that recent computational and experimental studies have demonstrated striking similarities in the caging dynamics of thermal fluids and the behavior of mechanically driven granular objects, including fluctuation or dynamic heterogeneity aspects [39–41].

VI. TRANSIENT LOCALIZATION AND ACTIVATED BARRIER HOPPING

We now consider beyond ideal MCT issues. Although there are many interesting and experimentally relevant aspects [8,10,12,42] (e.g., displacement of maximum restoring force, absolute yield stress, shear modulus, self-diffusion constant, shear viscosity), we study just four topics: the form of the nonequilibrium free energy, the (transient) localization length, the entropic barrier, and the mean activated hopping time.

A. Nonequilibrium free energy

Examples of the nonequilibrium free energy are shown in Fig. 8. The volume fraction for each object shape is adjusted to achieve a common barrier height of 5 k_BT. Based on this "calibration" the effective free energy curves are all very similar and the localization lengths are essentially identical. This conclusion is not sensitive to the precise value of the barrier height chosen to make the comparison. The only substantive difference is a modest shift of the barrier location outwards, and curvature softening, as the hard object becomes smoother. A theoretical basis for this simplicity has been suggested [24].

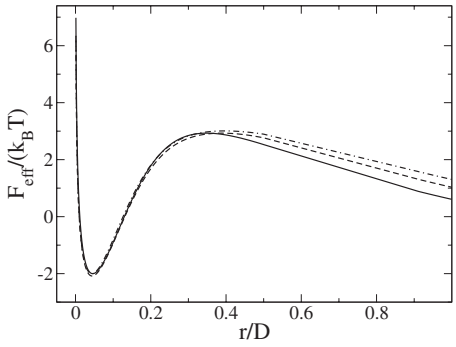

FIG. 8. Nonequilibrium free energy in units of the thermal energy as a function of normalized particle displacement for the three shapes at a common aspect ratio ($L/D=2$) with volume fractions adjusted so that the barrier height equals $5k_BT$. The required volume fractions are $\phi=0.505$ for the diatomic (solid curve), $\phi=0.605$ for the triatomic (dashed curve), and $\phi=0.677$ for the spherocylinder (dot-dashed curve). The triatomic and spherocylinder curves are vertically and horizontally shifted to align their localization lengths (in units of D) in order to demonstrate the high similarity for all three geometrical shapes.

B. Localization lengths

The (transient) localization length in units of the elementary excluded volume length scale, D, *along* the ideal glass boundary is shown in Fig. 9. A remarkably good collapse is found for the different shapes. The localization length increases roughly linearly with aspect ratio, perhaps indicative of r_{loc} being sensitive to the overall object size. If the volume fraction in the ideal glass is held constant then the localization length varies in a nonmonotonic manner with L/D (not shown) which reflects the shape of the ideal glass boundary.

The inset of Fig. 9 presents the localization length as a function of volume fraction for $L/D=1.5$ and 3 triatomics. A roughly exponential decrease with volume fraction is predicted as found for other systems [8,12]. Moreover, the average slope is only weakly sensitive to object shape or aspect ratio. Possible collapse of these curves based on the two measures of distance from the ideal glass line previously discussed [12], $\phi-\phi_C$ and $(\phi/\phi_C)-1$, was investigated. We find the collapse is not very good for the former measure of reduced volume fraction, but is quite good for the latter if a small vertical shift is applied to account for an L/D-dependent effective diameter (not plotted).

C. Entropic barrier

The magnitude of the α relaxation time is dominated by the entropic barrier height. Figure 10 shows representative

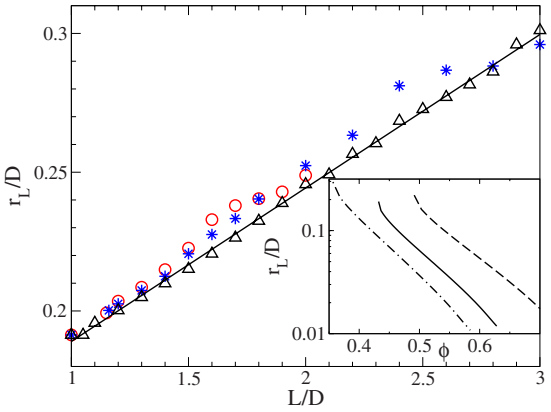

FIG. 9. (Color online) Localization length (in units of D) as a function of aspect ratio along the ideal glass boundary for the diatomic (circles), triatomic (stars), and spherocylinder (triangles). A linear fit to the spherocylinder results is shown. The inset presents in a log-linear format the volume fraction dependent localization length for the hard sphere (solid) and $L/D=1.5$ (dashed) and 3.0 (dot-dashed) triatomics.

results for its dependence on object shape and volume fraction. The main panel demonstrates that at fixed aspect ratio the volume fraction dependence for different objects is quite similar. The inset shows results for the triatomic and several aspect ratios. As expected, the barrier is a nonmonotonic function of aspect ratio. We have previously shown [12] for diatomics that the volume fraction dependence can be empirically well described as a critical power law, $F_B \propto (\phi - \phi_C)^{\nu}$, where $\nu \approx 2$ for all bond length to site diameter ratios. The same behavior is found to work rather well for barrier heights up to $\sim 10\ k_BT$ for triatomics and spherocylinders, $F_B \cong C(\phi/\phi_C - 1)^x$, where $x \sim 1.9-2.0$ and $C \sim 40-60$.

Figure 11 attempts a collapse of the barrier as a function of volume fraction for all shapes and several aspects ratios. For the modestly anisotropic $L/D=1.5$ case, the barriers of

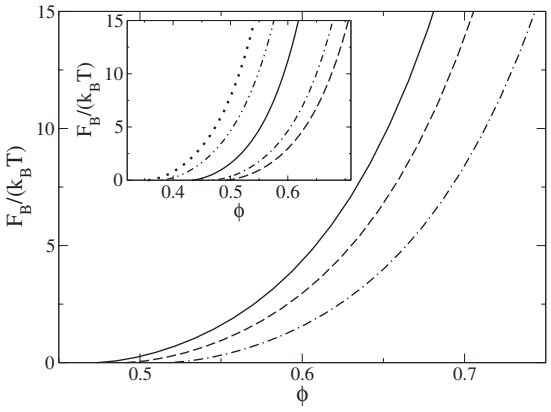

FIG. 10. Barrier height as a function of volume fraction for the diatomic (solid), triatomic (dashed), and spherocylinder (dot-dashed) at a common aspect ratio of $L/D=1.5$. The inset shows the barrier height as a function of volume fraction for a triatomic of $L/D=1$ (solid), 1.5 (dashed), 2.0 (dot-dashed), 2.8 (dot-dot-dashed) and 3.0 (large dots).

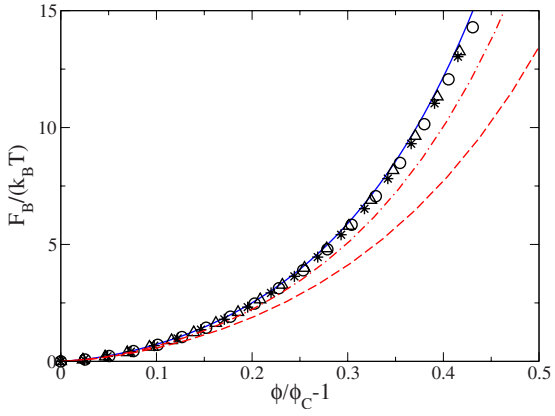

FIG. 11. (Color online) Barrier heights as a function of a normalized measure of the distance from the ideal glass boundary. Results are shown for the hard sphere (solid curve), diatomic (circles), triatomic (stars), and spherocylinder (triangles) for $L/D=1.5$, and the triatomic (dashed) and spherocylinder (dash-dot) at $L/D=3$.

all objects (including hard spheres) collapse based on a dimensionless volume fraction which quantifies the distance from the ideal glass boundary. This collapse holds well up to $L/D \sim 2$ (not shown), but with increasing aspect ratio deviations emerge. The limiting $L/D=3$ case is also shown, and the results neither overlap with their $L/D=1.5$ analogs, nor do the triatomic and spherocylinder curves collapse. In the representation of Fig. 11 the volume fraction dependence is weaker at $L/D=3$, and weakest for the triatomic. This highlights the important role of the smoothness or corrugation of the object in affecting packing and activated dynamics.

D. Mean hopping time and α relaxation

The mean barrier hopping time, which we identify with the single particle α relaxation time [10], has been computed based on Eq. (14). The nondimensionalizing elementary short time scale, $\tau_s \equiv \beta D^2 \zeta_s$, is in practice (weakly) shape and volume fraction dependent via the short time friction constant. Figure 12 shows results for the three shapes at two high volume fractions: 0.57 (roughly the empirical experimental kinetic glass transition volume fraction of hard spheres) and 0.62. At aspect ratios close to unity the relaxation times for different shapes closely overlap since their respective ideal glass boundaries superimpose almost perfectly (see Fig. 3). At larger aspect ratios a nonmonotonic variation is found which is shape specific. For $\phi=0.57$ the mean hopping time varies by 5 orders of magnitude for the diatomic, 7 orders of magnitude for the triatomic, and only 2 orders of magnitude for the spherocylinder. At $\phi=0.62$ the variations are larger of course, and the detailed shape of the volume fraction dependences also change. In this case the spherocylinder mean hopping time changes by roughly 4 orders of magnitude. Given quantitative knowledge of the short time scale, τ_s, a kinetic glass transition can be defined as when the hopping (α) time reaches an experimentally defined threshold beyond which relaxation is unobservable.

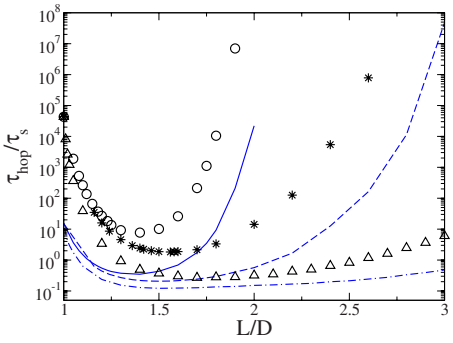

FIG. 12. (Color online) Mean barrier hopping time normalized by the elementary short relaxation time, τ_s, as a function of aspect ratio for the diatomic (circles), triatomic (stars), and spherocylinder (triangles) at a volume fraction of $\phi=0.62$. Analogous results for $\phi=0.57$ are shown as smooth curves for the diatomic (solid), triatomic (dashed), and spherocylinders (dot-dashed).

VII. SUMMARY AND DISCUSSION

Our theory for the ideal kinetic glass transition and activated barrier hopping dynamics of fluids of hard nonspherical objects [12] has been applied to several modestly anisotropic shapes. The role of bond length, aspect ratio, and degree of object smoothness has been established. For all shapes studied the ideal glass boundary is a nonmonotonic function of aspect ratio. As spherical symmetry is broken, the glass volume fractions increase linearly with aspect ratio with a slope that appears to be identical for the diatomic, triatomic, and spherocylinder. This behavior, including the *quantitative* value of the slope, is in remarkable agreement with the jamming phase diagram of granular ellipsoids [34]. Each shape displays a maximum glass volume fraction which occurs at larger values and aspect ratios as the object becomes smoother. These ideal glass boundaries appear to bracket the jamming curves of ellipsoids [34] and spherocylinders [23]. Theoretical suggestions for why nonthermal jamming and equilibrium kinetic ideal glass formation may be related have been suggested. Surprisingly, the amplitude of long wavelength density fluctuations is to a good approximation conserved along the ideal glass boundary of all shapes. A master curve for the localization length in units of the elementary excluded volume length is predicted with the precise value increasing linearly with aspect ratio.

Beyond the ideal glass boundary the nonequilibrium free energy acquires a localization well and barrier. Although its form for different shapes and aspect ratios is highly nonuniversal at fixed volume fraction, if different shapes are compared at constant entropic barrier height then a reasonably good collapse is found. The barriers of each object grow roughly quadratically with volume fraction as measured from the ideal glass boundary. Collapse of the volume fraction dependence of the barrier height is predicted for modest aspect ratios but increasingly fails as $L/D>2$. At fixed volume fraction the mean hopping times are nonmonotonic functions of aspect ratio. The specific form of the dependence, and order of magnitude variation, is distinct for each shape. Although not explored in this paper, many other aspects can be studied [12], including the role of object shape on transport coefficients, shear modulus, yield stress, and dynamic heterogeniety effects [10]. Some of our predictions should be amenable to testing via computer simulation. Advances in the synthesis of nonspherical colloids are proceeding rapidly [2,43–46] and we anticipate will allow confrontation of the theory with experiment in the near future.

Finally, a variety of additional systems and questions can be addressed using our approach. Problems under present study include long rigid rods and the relationship of the ideal glass boundary to the nematic and jamming transition boundaries [47], thin disks in both the isotropic and discotic liquid crystalline state [47], and hard compact (three-dimensional-like) molecular colloids of variable size and shape [48], as recently fabricated experimentally [2,43]. The present approach is not limited to hard objects. As done for spheres, intermolecular attractions can be added within the site level description to study the role of colloid shape on gelation and its competition with vitrification [13], and activated barrier hopping dynamics under both quiescent [14] and stressed conditions [49,50].

ACKNOWLEDGMENTS

This work was supported by the United States Department of Energy, Division of Materials Sciences, through the Frederick Seitz Materials Research Laboratory at UIUC funded by Grant No. DEFG02-91ER45439. K.S.S. thanks Sal Torquato for correspondence and discussions concerning jamming, and Alexander Donev for sending the hard ellipsoid simulation data in Fig. 7.

[1] See, for example, K. L. Ngai, J. Non-Cryst. Solids **275**, 7 (2000); C. A. Angell, K. L. Ngai, G. B. McKenna, P. F. McMillan, and S. W. Martin, J. Appl. Phys. **88**, 3113 (2000); M. D. Ediger, C. A. Angell, and S. D. Nagel, J. Phys. Chem. **100**, 13200 (1996).

[2] S. C. Glotzer, M. J. Solomon, and N. A. Kotov, AIChE J. **50**, 2978 (2004); A. van Blaaderen, Nature (London) **439**, 545 (2006); S. C. Glotzer, M. A. Horsch, C. R. Iacovella, Z. Zhang, E. R. Chan, and X. Zhang, Curr. Opin. Colloid Interface Sci. **10**, 287 (2005).

[3] W. Götze in Liquids, *Freezing and the Glass Transition*, edited by J. P. Hansen, D. Levesque and J. Zinn-Justin, (North-Holland, Amsterdam, 1991); W. Götze and L. Sjörgen, Rep. Prog. Phys. **55**, 241 (1992); M. Fuchs, Transp. Theory Stat. Phys. **24**, 855 (1995).

[4] S.-H. Chong, and W. Götze, Phys. Rev. E **65**, 041503 (2002); **65**, 051201 (2002).

[5] R. Schilling, Phys. Rev. E **65**, 051206 (2002); C. Theis, F.

Sciortino, A. Latz, R. Schilling, and P. Tartaglia, *ibid.* **62**, 1856 (2000); M. Letz, R. Schilling, and A. Latz, *ibid.* **62**, 5173 (2000).
[6] T. Theenhaus, M. P. Allen, M. Letz, A. Latz, and R. Schilling, Eur. Phys. J. E **8**, 269 (2002).
[7] A. J. Moreno, S.-H Chong, W. Kob, and F. Sciortino, J. Chem. Phys. **123**, 204505 (2005); S.-H. Chong, A. J. Moreno, F. Sciortino, and W. Kob, Phys. Rev. Lett. **94**, 215701 (2005).
[8] K. S. Schweizer and E. J. Saltzman, J. Chem. Phys. **119**, 1181 (2003); E. J. Saltzman and K. S. Schweizer, *ibid.* **119**, 1197 (2003).
[9] K. S. Schweizer, J. Chem. Phys. **123**, 244501 (2005).
[10] E. J. Saltzman and K. S. Schweizer, J. Chem. Phys. **125**, 044509 (2006); Phys. Rev. E **74**, 061501 (2006).
[11] K. S. Schweizer and E. J. Saltzman, J. Phys. Chem. B **108**, 19729 (2004).
[12] G. Yatsenko and K. S. Schweizer, J. Chem. Phys. **126**, 014505 (2007).
[13] Y.-L. Chen and K. S. Schweizer, J. Chem. Phys. **120**, 7212 (2004).
[14] Y.-L. Chen, V. Kobelev, and K. S. Schweizer, Phys. Rev. E **71**, 041405 (2005).
[15] K. S. Schweizer and E. J. Saltzman, J. Chem. Phys. **121**, 1984 (2004).
[16] F. T. Oyerokun and K. S. Schweizer, J. Chem. Phys. **123**, 224901 (2005).
[17] E. J. Saltzman and K. S. Schweizer, J. Phys.: Condens. Matter **19**, 205123 (2007).
[18] K. Chen and K. S. Schweizer, J. Chem. Phys. **126**, 014904 (2007).
[19] K. Chen and K. S. Schweizer, Phys. Rev. Lett. **98**, 167802 (2007).
[20] K. Chen and K. S. Schweizer, Europhys. Lett. **79**, 26006 (2007).
[21] A. Donev, I. Cisse, D. Sachs, E. A. Variano, F. H. Stillinger, R. Connelly, S. Torquato, and P. M. Chaikin, Science **303**, 990 (2004).
[22] W. Man, A. Donev, F. H. Stillinger, M. T. Sullivan, W. B. Russel, D. Heeger, S. Inati, S. Torquato, and P. M. Chaikin, Phys. Rev. Lett. **94**, 198001 (2005).
[23] S. R. Williams and A. P. Philipse, Phys. Rev. E **67**, 051301 (2003).
[24] K. S. Schweizer and G. Yatsenko, J. Chem. Phys. (to be published).
[25] D. Chandler and H. C. Andersen, J. Chem. Phys. **57**, 1930 (1972); D. Chandler, *Studies in Statistical Mechanics*, edited by J. L. Lebowitz and E. W. Montroll, (North Holland, Amsterdam, 1982), Vol. 8, p. 275.
[26] K. S. Schweizer and J. G. Curro, Adv. Chem. Phys. **98**, 1 (1997).
[27] Y.-L. Chen and K. S. Schweizer, Langmuir **18**, 7354 (2002); J. Phys. Chem. B **108**, 6687 (2004).
[28] J.-P. Hansen and I. R. McDonald, *Theory of Simple Liquids*, 3rd ed., (Academic Press, New York, 2006).
[29] I. Pagonabarraga and M. E. Cates, Europhys. Lett. **55**, 348 (2001).
[30] J. C. Pedersen, Adv. Colloid Interface Sci. **70**, 171 (1997).
[31] T. R. Kirkpatrick and P. G. Wolynes, Phys. Rev. A **35**, 3072 (1987).
[32] H. A. Kramers, Physica (Amsterdam) **7**, 284 (1940).
[33] K. S. Schweizer, M. Fuchs, G. Szamel, M. Guenza, and H. Tang, Macromol. Theory Simul. **6**, 1037 (1997).
[34] P. M. Chaikin, A. Donev, W. Man, F. H. Stillinger, and S. Torquato, Ind. Eng. Chem. Res. **45**, 6960 (2006).
[35] A. Donev, R. Connelly, F. H. Stillinger and S. Torquato, Phys. Rev. E **75**, 051304 (2007).
[36] E. A. J. F. Peters, M. Kollmann, T. M. A. O. M. Barenbrug, and A. P. Philipse, Phys. Rev. E **63**, 021404 (2001).
[37] S. Torquato (private communication).
[38] S. Torquato, *Random Heterogeneous Materials: Microstructure and Macroscopic Properties* (Springer, New York, 2002).
[39] A. S. Keys, A. R. Abate, S. C. Glotzer, and D. J. Durian, Nat. Phys. **3**, 260 (2007).
[40] A. R. Abate and D. J. Durian, Phys. Rev. E **74**, 031308 (2006).
[41] P. M. Reis, R. A. Ingale, and M. D. Shattuck, Phys. Rev. Lett. **98**, 188301 (2007).
[42] V. Kobelev and K. S. Schweizer, Phys. Rev. E **71**, 021401 (2005).
[43] V. N. Manoharan, M. T. Elseser, and D. J. Pine, Science **301**, 483 (2003); V. N. Manoharan, Solid State Commun. **139**, 557 (2006).
[44] E. B. Mock, H. De Bruyn, B. S. Hawkett, R. G. Gilbert, and C. F. Zukoski, Langmuir **22**, 4137 (2006).
[45] P. M. Johnson, C. M. van Kats, and A. van Blaaderen, Langmuir **21**, 11510 (2005).
[46] T. Sun and Y. Xia, Science **298**, 2176 (2002).
[47] G. Yatsenko and K. S. Schweizer (unpublished).
[48] M. Tripathy and K. S. Schweizer (unpublished).
[49] V. Kobelev and K. S. Schweizer, J. Chem. Phys. **123**, 164902 (2005).
[50] V. Gopalakrishnan, K. S. Schweizer, and C. F. Zukoski, J. Phys.: Condens. Matter **18**, 11531 (2006).